

**Impurity effects on Dirac modes in graphene armchair nanoribbons**Yuriy G. Pogorelov <sup>\*</sup>*IFIMUP-IN, Departamento de Física e Astronomia, Universidade do Porto, Porto, 4169-007 Porto, Portugal*Vadim M. Loktev <sup>†</sup>*N. N. Bogolyubov Institute of Theoretical Physics, NAS of Ukraine, 03143 Kyiv, Ukraine*

(Received 15 September 2022; accepted 8 November 2022; published 5 December 2022)

We consider finite ribbons of graphene with armchair orientation of their edges to study in detail impurity effects on specific Dirac-like modes. In the framework of the Anderson hybrid model of impurity perturbation, a possibility for Mott localization and for opening of a mobility gap under local impurity perturbations is found and analyzed as a function of the model parameters: the impurity energy level, its hybridization with the host Dirac modes, and the impurity concentration. Special attention is paid to the interplay between impurity disorder and spin-orbit splitting of the host spectrum for the purpose of tunable metal-insulator phase transitions.

DOI: [10.1103/PhysRevB.106.224202](https://doi.org/10.1103/PhysRevB.106.224202)**I. INTRODUCTION**

Between electronic properties of a two-dimensional (2D) graphene layer, the presence of linear gapless quasiparticle modes, or 2D Dirac modes, is especially notable by defining unusual physical effects in graphene [1–3]. These modes are also a source for even finer, one-dimensional (1D) Dirac modes in graphene nanoribbons [4–6] with special orientation of their edges and special adjustment of their atomic width [7].

A broad family of Dirac semimetals is of great interest for modern electronics, in particular, their behavior under doping by different impurities and the resulting restructuring of the quasiparticle spectrum. Comparing with the known impurity effects in common semiconductors and in 2D graphene, the doped graphene nanoribbons can be expected to permit even higher sensitivity to various external controls, and their study may deepen our general knowledge of disorder physics.

This work continues our recent study of impurity effects in graphene nanoribbons [8] which has demonstrated different sensibility to the impurity disorder: almost absent in zigzag graphene nanoribbons (ZGNRs), known also as topological protection, but already found in some armchair graphene nanoribbons (AGNRs), namely, in those presenting Dirac-like modes in the electronic spectra. However, their study was restricted to the simplest Lifshitz isotropic model of impurity perturbation (more adequate for substitutional centers), permitting only quasiparticle localization near Dirac zero points. Therefore, looking for other impurity resonances of physical interest, we focus below on the more flexible Anderson hybrid *s-d* model, better describing impurity adatoms. In this course, we find various regimes of spectrum restructuring

as a function of perturbation parameters and compare the obtained results with known such effects in other electronic materials.

The following consideration begins from the description of AGNR and its spectral structure in terms of the second quantization Hamiltonian (Sec. II) and the related Green functions (GFs, Sec. III). The perturbation of Hamiltonian by impurity adatoms within the Anderson hybrid model is introduced in Sec. IV, giving the solutions for perturbed GFs in the T-matrix form and the checks for Mott localization of perturbed quasiparticles. The analysis of possible electronic phase states and transitions between them in a doped AGNR as a function of perturbation parameters is developed in Sec. V and compared with the known behaviors of analogous electronic materials. A special consideration of such transitions under an interplay of impurity perturbations and different types of spin-orbit coupling, including its tuning by external fields, is given in Sec. VI. The final discussion of the obtained results with suggestions for their possible practical use is presented in Sec. VII. A more detailed analysis of the solutions for 1D modes, beyond the T-matrix framework, is done in the Appendix.

**II. HAMILTONIAN, EIGENSTATES, AND ENERGY SPECTRUM**

The graphene armchair nanoribbon can be seen as a sequence of  $N$  segments where each segment is a slant stack of  $M$  layers (collinear between the segments) and each layer consists of two atomic sites (of graphene *a* and *b* types, see Fig. 1). The respective local electronic states in the  $m$ th layer of the  $n$ th segment are generated by the local operators  $a_{n,m}^\dagger$  and  $b_{n,m}^\dagger$ . Longitudinal translational invariance is imposed through the Born–von Karman closure of the  $N$ th to the first segment. For an AGNR with  $M$  layers ( $M$ -AGNR) and the nearest-neighbor

<sup>\*</sup>ypogorel@fc.up.pt<sup>†</sup>vloktev@bitp.kiev.ua

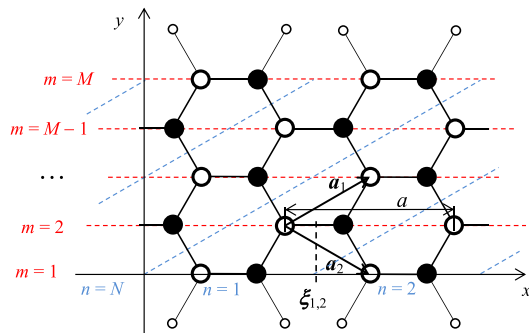


FIG. 1. Graphene nanoribbon with armchair orientation of its edges. Blue dashed lines delimit slant segments  $n = 1, \dots, N$ . Each segment extends along the graphene elementary translation vector  $\mathbf{a}_1$  and includes  $m = 1, \dots, M$  layers (red dashed lines) with  $a$ -type (white) and  $b$ -type (black) atomic sites. The sequence of segments has its longitudinal period  $a = |\mathbf{a}_1 + \mathbf{a}_2|$ . The carbon dangling bonds at the edges are passivated by hydrogens (small circles).

hopping  $t$ , the related tight-binding Hamiltonian reads

$$H_{tb} = t \left\{ \sum_{n=1}^N \left[ \sum_{m=2}^M a_{n,m}^\dagger (b_{n,m} + b_{n-1,m+1} + b_{n,m-1}) + a_{n,1}^\dagger (b_{n,1} + b_{n-1,2}) \right] + \sum_{m=1}^{M-1} a_{1,m}^\dagger b_{N,m+1} + \text{H.c.} \right\}. \quad (1)$$

The last sum in Eq. (1) just generates the longitudinal translation invariance and suggests the Fourier-transform to 1D-wave operators. The longitudinal coordinates of  $a$  and  $b$  sites in units of the longitudinal period  $a = |\mathbf{a}_1 + \mathbf{a}_2|$  define this transform as

$$\alpha_{k,m} = \frac{1}{\sqrt{N}} \sum_{n=1}^N e^{i(2\pi k/N)(\xi_{n,m}-1/6)} a_{n,m},$$

$$\beta_{k,m} = \frac{1}{\sqrt{N}} \sum_{n=1}^N e^{i(2\pi k/N)(\xi_{n,m}+1/6)} b_{n,m}, \quad (2)$$

where  $\xi_{n,m} = n + (m+1)/2$  is the longitudinal coordinate of the center of the  $m$ th layer from  $n$ th segment (see an example in Fig. 1). This readily diagonalizes the Hamiltonian, Eq. (1), in the  $k$  numbers. If the AGNR is macroscopically long,  $N \rightarrow \infty$ , one can pass to a quasicontinuous momentum variable:  $2\pi k/N \rightarrow k$  (measured in  $a^{-1}$  units). Also, for simplicity, the energy  $\varepsilon$  will be measured in units of  $t$ .

Then the system dynamics in the transversal  $m$  index can be considered at a fixed longitudinal  $k$  momentum, and the overall spectrum structure results are qualitatively defined by the AGNR width  $M$ . In the known analytic approach by Wakabayashi *et al.* [7,9,10],  $2M$  eigenstates at given  $k$  are taken as running  $k$  waves superposed by standing waves in the transversal  $q$  momentum, subject to the open-edge condition (reaching a node when continued by a half-period beyond an AGNR edge). Namely, they are pairs of standing waves with discrete momentum values:

$$q_j = \frac{\pi j}{M+1}, \quad j = 1, \dots, M, \quad (3)$$

being just the combinations (symmetric and antisymmetric in  $a$  and  $b$  sites) of 1D-projected graphene states.

The related eigenenergies are simple uniform 1D projections of the 2D graphene spectrum for transversal momentum values  $q_j$  by Eq. (3):

$$\varepsilon_{j,k} = \sqrt{1 + 4 \cos \frac{k}{2} \cos q_j + 4 \cos^2 q_j}, \quad (4)$$

for conduction subbands (and  $-\varepsilon_{j,k}$  for valence subbands). The 1D Brillouin zone (BZ) for all the  $2M$  subbands is defined within the  $0 \leq k \leq 2\pi$  range, and the respective secular determinant reads

$$\det(\varepsilon - \hat{H}) = \prod_{j=1}^M (\varepsilon^2 - \varepsilon_{j,k}^2). \quad (5)$$

The eigenstate associated to the  $(j, k)$  mode is a combination of the running  $k$  wave and the standing  $q_j$  wave [10] with its amplitudes on  $a$  and  $b$  sites in the  $m$  layer:

$$A_m^{(j,k)} = -\frac{e^{-i\varphi_{j,k}}}{\sqrt{M+1}} \sin m q_j,$$

$$B_m^{(j,k)} = \frac{e^{i\varphi_{j,k}}}{\sqrt{M+1}} \sin m q_j, \quad (6)$$

where the phase is defined by the relation

$$\varphi_{j,k} = \frac{1}{2} \arctan \frac{\sin \frac{k}{2}}{\cos \frac{k}{2} + 2 \cos q_j} + \frac{k}{6}. \quad (7)$$

The standing waves are orthonormalized through the relations

$$\sum_{j=1}^M \sin m q_j \sin m' q_j = \frac{M+1}{2} \delta_{m,m'},$$

$$\sum_{m=1}^M \sin m q_j \sin m q_{j'} = \frac{M+1}{2} \delta_{j,j'}. \quad (8)$$

Then we construct the eigenmode operators  $\psi_{\pm j,k}$  from the wave operators  $\alpha_{m,k}$  and  $\beta_{m,k}$  by Eq. (2) in order to reproduce the mode amplitudes by Eq. (6):

$$\psi_{\pm j,k} = \frac{1}{\sqrt{M+1}} \sum_{m=1}^M \sin m q_j (e^{i\varphi_{j,k}} \beta_{m,k} e^{-i\varphi_{j,k}} \alpha_{m,k}). \quad (9)$$

In their basis, the Hamiltonian, Eq. (1), turns fully diagonal:

$$H_{tb} = \sum_{j,k} \varepsilon_{j,k} (\psi_{j,k}^\dagger \psi_{j,k} - \psi_{-j,k}^\dagger \psi_{-j,k}). \quad (10)$$

By inversion of Eqs. (2) and (9), the local operators can be expanded in the eigenmode operators:

$$a_{n,m} = \frac{1}{\sqrt{(M+1)N}} \sum_{j,k} e^{i(k\xi_{n,m} - \varphi_{j,k})} \sin m q_j (\psi_{-j,k} - \psi_{j,k}),$$

$$b_{n,m} = \frac{1}{\sqrt{(M+1)N}} \sum_{j,k} e^{i(k\xi_{n,m} + \varphi_{j,k})} \sin m q_j (\psi_{-j,k} + \psi_{j,k}), \quad (11)$$

which is helpful for the next treatment of AGNR perturbations by local impurity centers.

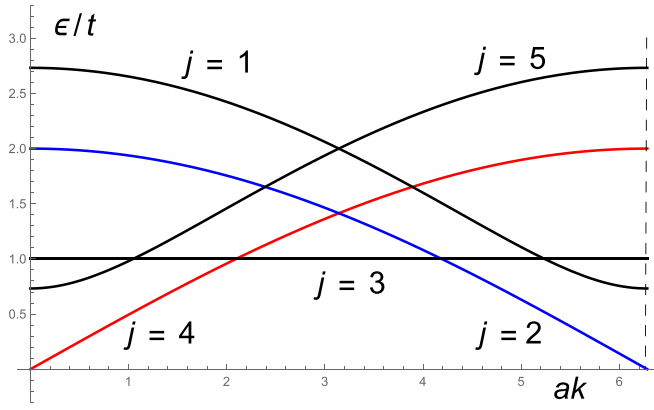


FIG. 2. Energy-band dispersion in 5-AGNR [ $\nu = 2$  by Eq. (12)], showing the Dirac-like modes with  $j = 2, 4$ .

The notable feature of the spectrum by Eq. (4) is that it contains gapless modes if the AGNR width satisfies a special condition [7]:

$$M + 1 = 3\nu, \quad \nu = 1, 2, \dots \quad (12)$$

For such  $M = 3\nu - 1$ , the mode with  $j = 2\nu$  reaches zero energy at the BZ edge  $k = 0$  as

$$\varepsilon_{2\nu,k} = 2 \left| \sin \frac{k}{4} \right| \approx \frac{|k|}{2} \quad (13)$$

(see Fig. 2), and the mode with  $j = \nu$  reaches zero energy at the opposite BZ edge  $k = 2\pi$  as

$$\varepsilon_{\nu,k} = 2 \left| \cos \frac{k}{4} \right| \approx \frac{|k - 2\pi|}{2}. \quad (14)$$

The dispersion laws by Eqs. (13) and (14) formally coincide with the standard linear dispersion near the Dirac points of 2D graphene; hence they can be seen as definitions of effective 1D Dirac points in  $(3\nu - 1)$ -AGNR spectra. All other modes there (with  $j \neq \nu, 2\nu$ ) have finite energy gaps.

### III. GREEN FUNCTIONS AND OBSERVABLES

The following consideration goes in the framework of two-time GFs [11,12], defined by their Fourier transforms:

$$\langle\langle A|B \rangle\rangle_\varepsilon = \frac{i}{\pi} \int_0^\infty dt e^{it(\varepsilon+i0)} \langle\{A(t), B(0)\}\rangle, \quad (15)$$

where  $A(t) = e^{iHt} A e^{-iHt}$  is a Heisenberg picture operator for the system Hamiltonian  $H$ ,  $\{.,.\}$  is the anticommutator, and  $\langle\langle \dots \rangle\rangle$  is the quantum-statistical average. In what follows, the GF's energy subindex is mostly omitted.

Practical calculation of GFs is done through the general equation of motion:

$$\varepsilon \langle\langle A|B \rangle\rangle = \langle\{A(0), B(0)\}\rangle + \langle\langle [A, H]|B \rangle\rangle, \quad (16)$$

involving the commutator  $[.,.]$ . So found GFs generate the physical observable quantities (the averages of operator products) through the spectral relation

$$\langle AB \rangle = \frac{1}{\pi} \text{Im} \int_0^\infty \langle\langle B|A \rangle\rangle_\varepsilon d\varepsilon. \quad (17)$$

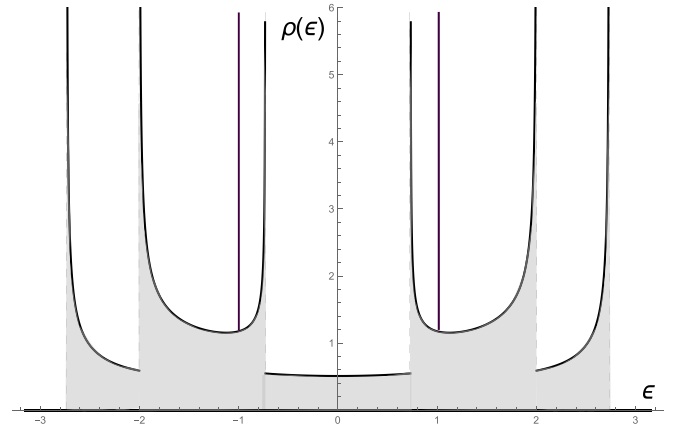


FIG. 3. Density of states in 5-AGNR. Almost constant value  $\approx 4/(3\pi)$  within the low-energy range,  $|\varepsilon| \leq \sqrt{3} - 1$ , comes from the Dirac-like ( $j = 2, 4$ ) subbands.

In the present case, the system electronic properties can be obtained from the  $2M \times 2M$  GF matrix  $\hat{G}(k, k')$  with its matrix elements  $G_{j,j'}(k, k') \equiv \langle\langle \psi_{j,k} | \psi_{j',k'}^\dagger \rangle\rangle$  built from the eigenmode operators by Eq. (9) where the  $j$  indices count the transversal momenta as by Eq. (3) and also their opposites  $-j$  ( $2M$  altogether).

For the unperturbed AGNR system with its diagonal Hamiltonian, Eq. (10), the above-defined GF matrix results are also diagonal:  $G_{j,j'}^{(0)}(k, k') = \delta_{j,j'} \delta_{k,k'} G_{j,k}^{(0)}(\varepsilon)$ , with its diagonal elements called propagators,

$$G_{j,k}^{(0)}(\varepsilon) = \frac{1}{\varepsilon - \varepsilon_{j,k}}. \quad (18)$$

They define an important observable, the density of quasi-particle states (DOS), as a sum  $\rho(\varepsilon) = \sum_{j=1}^M \rho_j(\varepsilon)$ , where a partial contribution from  $(j, -j)$  subbands is

$$\rho_j(\varepsilon) = \frac{2}{\pi} \sum_k \text{Im} [G_{j,k}^{(0)}(\varepsilon) + G_{-j,k}^{(0)}(\varepsilon)] \quad (19)$$

(including the implicit factor 2 for electron spins). Using Eq. (18) and passing from the sum in  $k$  to the integral,

$$\frac{1}{N} \sum_k f(k) = \frac{1}{2\pi} \int_0^{2\pi} f(k) dk, \quad (20)$$

gives this contribution as

$$\rho_j(\varepsilon) = \frac{8|\varepsilon|}{\pi(M+1) \sqrt{(\varepsilon^2 - \varepsilon_{-,j}^2)(\varepsilon_{+,j}^2 - \varepsilon^2)}}, \quad (21)$$

where  $\varepsilon_{\pm,j} = 1 \pm 2 \cos q_j$  are the  $j$ th subband energy limits.

In particular, for the most relevant here Dirac-like modes with  $\varepsilon_{+,2\nu} = \varepsilon_{-,2\nu} = 2$ ,  $\varepsilon_{+,2\nu} = \varepsilon_{-,2\nu} = 0$ , we have

$$\rho_\nu(\varepsilon) = \rho_{2\nu}(\varepsilon) = \frac{4}{3\pi\nu\sqrt{1 - (\varepsilon/2)^2}}, \quad (22)$$

so the low-energy DOS results are almost constant:  $\rho(\varepsilon) \approx \rho(0) = 8/(3\pi\nu)$  at  $|\varepsilon| \ll 1$ , as seen in the case of 5-AGNR presented in Fig. 3.

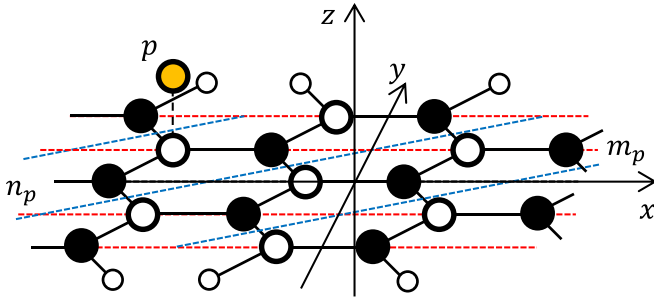


FIG. 4. Position  $p$  of a top impurity adatom over an  $a$  site in  $m_p$  layer from  $n_p$  segment of 5-AGNR.

#### IV. IMPURITY PERTURBATIONS

The local impurity perturbations in graphene nanoribbons of both zigzag and armchair types were recently considered within two basic impurity models: the one-parameter Lifshitz model (LM) [13], more adequate for substitutional impurities, and the two-parameter Anderson hybrid model (AM) [14], for impurity adatoms [8]. For zigzag structures, the overall conclusion was about their eigenmode stability (topological protection) against quasiparticle localization by the impurity disorder, both in LM and AM models. However, such localization was found in AGNRs with LM impurities, though reduced in that case to a narrow vicinity of the Dirac point (zero energy). But this already opens a possibility for Mott's metal/insulator phase transitions in a nanosystem and generates the next interest for studying AGNR behavior under more diversified AM perturbations. In the latter case, a more complicated intermittence of conducting and localized states in other ranges of energy spectrum and a broader variety of related phase states for this 1D system can be expected. Then it would be also of interest to compare such effects with the known analogs for 3D and 2D electronic systems under impurity disorder.

The following consideration is focused on special  $(3\nu - 1)$  AGNRs and restricted to only their Dirac-like modes. Since these modes with  $j = \nu$  and  $2\nu$  give identical and independent contributions to the spectrum, one can next focus on a single Dirac-like mode, say  $j = 2\nu$ , then denoting  $\psi_{2\nu,k} \equiv \psi_{+,k}$  and  $\psi_{-2\nu,k} \equiv \psi_{-,k}$ . Consequently, the above-introduced  $\hat{G}(k, k')$  matrix gets reduced to the  $2 \times 2$  form in the basis of  $\psi_{\pm,k}$  operators. In particular, the nonperturbed solution, Eq. (18), presents here as  $\hat{G}^{(0)}(k, k') = \delta_{k,k'}(\varepsilon - \varepsilon_k \hat{\sigma}_3)^{-1}$  with  $\varepsilon_k \equiv \varepsilon_{2\nu,k}$  by Eq. (13) and the Pauli matrix  $\hat{\sigma}_3$  in  $\pm$  indices.

Then we consider the impurity adatoms location restricted to the simplest top positions:  $p_a$  over an  $a$ -type host atom in  $m_p$  layer from an  $n_p$  segment (see Fig. 4) or  $p_b$  over a  $b$ -type host atom. In these notations, the AM perturbation Hamiltonian reads

$$H_{AM} = \sum_p \left\{ \varepsilon_{res} c_p^\dagger c_p + \frac{\omega}{\sqrt{3\nu N}} \sum_k \left[ \sin \frac{\pi m_p}{3} \times e^{i(k\xi_p \mp \phi_k)} c_p^\dagger (\psi_{-,k} \mp \psi_{+,k}) + \text{H.c.} \right] \right\}, \quad (23)$$

where a local impurity operator  $c_p$  with its resonance level  $\varepsilon_{res}$  is coupled to the Dirac-like modes  $\pm \varepsilon_k$  through the hybridiza-

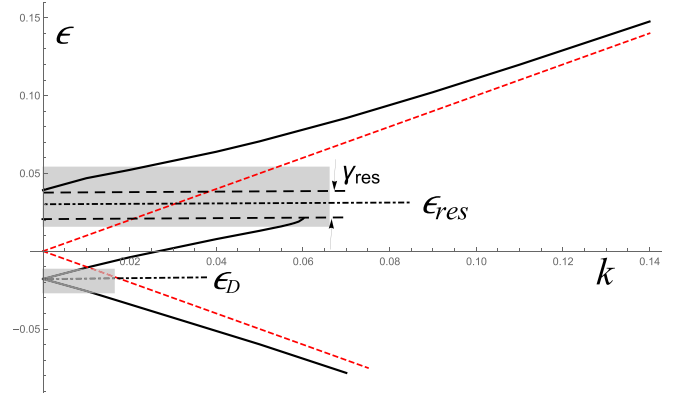


FIG. 5. Dispersion law for the Dirac-like modes in 5-AGNR having AM impurities with their parameters  $\varepsilon_{res} = 0.03$ ,  $\omega = 0.3$ , and concentration  $c = 0.02$ . For comparison, the unperturbed Dirac-like modes are shown by the red dashed lines.

tion  $\omega$  with the neighbor host atom at the longitudinal position  $\xi_{n_p, m_p} - 1/6$  for its  $a$  type as in Fig. 4 (or  $\xi_{n_p, m_p} + 1/6$  for its  $b$  type).

Then the complete Hamiltonian  $H_{tb} + H_{AM}$  generates a perturbation of the GF matrix:  $\hat{G}^{(0)} \rightarrow \hat{G}$ . In its simplest form, this is given by the T-matrix approximation:

$$\hat{G} = (\varepsilon - c\hat{T}(\varepsilon) - \varepsilon_k \hat{\sigma}_3)^{-1}, \quad (24)$$

where  $c = (2MN)^{-1} \sum_p 1$  is the impurity concentration and the T matrix in this case results diagonal:

$$\hat{T}(\varepsilon) \equiv T(\varepsilon) = \frac{\omega^2}{2} \left( \varepsilon - \varepsilon_{res} - \frac{i\omega^2}{4f\sqrt{1 - (\varepsilon/2)^2}} \right)^{-1}. \quad (25)$$

Then the modified dispersion law  $\tilde{\varepsilon}_k$  follows from the standard GF secular equation  $\text{Re}[\det(\hat{G})^{-1}] = 0$  [15] as

$$\tilde{\varepsilon}_k = \sqrt{\varepsilon_k^2 + [c \text{Im} T(\varepsilon)]^2 + c \text{Re} T(\varepsilon)}, \quad (26)$$

and its solution for 5-AGNR at the choice of AM impurity parameters  $\varepsilon_{res} = 0.03$  and  $\omega = 0.3$ , corresponding to Cu adatoms in the top position [16], is presented in Fig. 5. Here the characteristic impurity effects are seen as

(1) the shift of the Dirac point from its initial zero energy position down to

$$\varepsilon_D \equiv \tilde{\varepsilon}_{k=0} \approx \frac{\varepsilon_{res} - \sqrt{\varepsilon_{res}^2 + 2c\omega^2}}{2}, \quad (27)$$

(2) the resonance splitting between the initial linear  $\varepsilon_k$  law and the impurity resonance level  $\varepsilon_{res}$  until its vicinity of width

$$\gamma_{res} \approx \omega \sqrt{\frac{c - c_0}{2}}, \quad (28)$$

where  $c_0 \sim \omega^2/(8\nu^2)$  is the critical concentration value for this splitting to appear.

Also an anomalous negative dispersion formally appears inside this vicinity, at  $|\varepsilon - \varepsilon_{res}| \lesssim \gamma_{res}$ , but this range occurs unphysical when validity of the modified dispersion law is checked with the Ioffe-Regel-Mott (IRM) criterion for con-

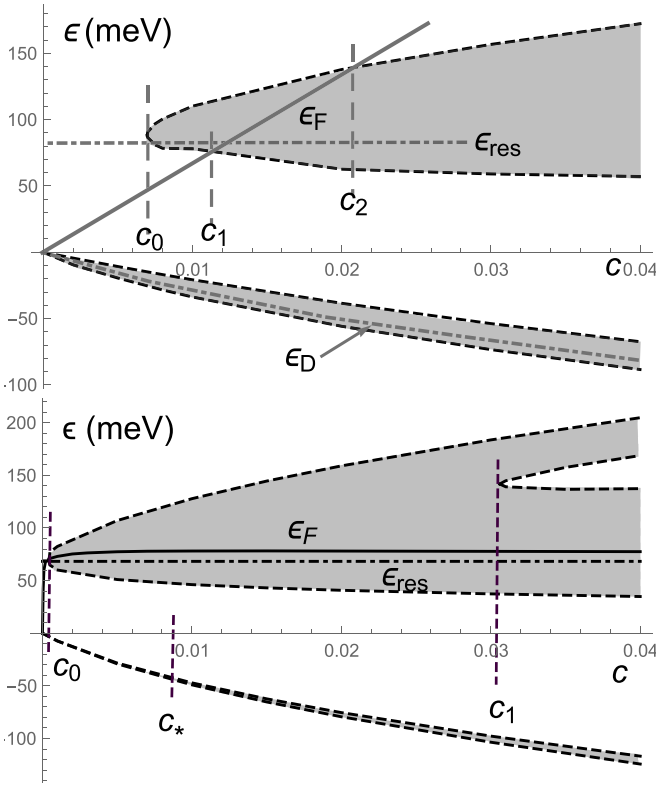


FIG. 6. Upper panel: Mobility gaps (in meV scale) in function of impurity concentration  $c$  at the choice of AM parameters as in Fig. 5. Special concentration values respectively refer  $c_0$  to opening of mobility gap near the resonance level  $\epsilon_{res}$ ,  $c_1$  to metal/insulator, and  $c_2$  to insulator/metal transitions (see below). Lower panel: Analogous developments for the same impurities in 2D graphene. Note here opening of a spectrum quasigap inside the mobility gap at  $c_1$ , absent in AGNR.

ducting states [17,18]:

$$k \frac{\partial \tilde{\epsilon}_k}{\partial k} \gtrsim c \operatorname{Im} T(\tilde{\epsilon}_k). \quad (29)$$

This simply means that the quasiparticle lifetime (inverse of the right-hand side) is longer than its oscillation period (inverse of the left-hand side), and such quasiparticles are conductive indeed; otherwise they are localized near impurity sites. The explicit form of the IRM criterion for the dispersion law by Eq. (26) and the T matrix by Eq. (25) reads

$$\frac{2}{\frac{\partial}{\partial \epsilon} \ln \{\operatorname{Re} [\epsilon - cT(\epsilon)]^2\}} \gtrsim c \operatorname{Im} T. \quad (30)$$

All the energy ranges where this inequality does not hold are attributed to localized states, so the dispersion law by Eq. (26) for conducting states does not apply there. The mobility edges between conducting and localized states can be estimated as the  $\epsilon$  values that make the relation of Eq. (30) an equality. The results of such numerical estimation at the choice of AM parameters as for Cu top impurities are shown in Fig. 6. They demonstrate formation of two mobility gaps (ranges of localization), one around  $\epsilon_{res}$  and another around  $\epsilon_D$ . Their width grows with the impurity concentration  $c$ : the first as  $\sim 2\gamma_{res}(c)$  by Eq. (28) and the second as  $\gamma_D \approx c\omega^4/[8v(\epsilon_D - \epsilon_{res})^2]$ .

The validity of the above T-matrix description is confirmed with an additional check beyond the frame of this simplest approximation (see in Appendix).

An important issue for such disordered AGNRs is how the positions of mobility edges compare with that of the Fermi level vs impurity concentration,  $\epsilon_F(c)$ . The latter results from an extra amount of  $c$  charge carriers by impurities filled into the relevant subbands:

$$\int_0^{\epsilon_F(c)} \rho(\epsilon) d\epsilon = c. \quad (31)$$

Notably, the above-indicated low-energy DOS,  $\rho(\epsilon) \approx \rho(0) = 8/(3\pi v)$ , holds its constancy even under impurity disorder, as seen from stability of Eq. (22) at passing  $\epsilon \rightarrow \epsilon - cT(\epsilon)$  since  $|\epsilon - cT(\epsilon)| \ll 1$  for all  $|\epsilon| \ll 1$ , one of the main specifics of this 1D-like system.

Then from Eq. (31) we come to the relation  $\epsilon_F(c) \approx c/\rho(0)$ . This behavior superposed onto the diagram of mobility gaps in Fig. 6 shows a possibility for  $\epsilon_F$  to cross the mobility edges near  $\epsilon_{res}$ , both into and out of this mobility gap. Then an intermittency of the related metal/insulator transitions (MIT) can be expected.

It is of interest to compare these AGNR results and their analogs for the same impurities in 2D graphene (Fig. 6, lower panel). Besides a general similarity of two pictures, they also present substantial differences. First of all, the estimated critical concentration for localization on Cu impurities in 5-AGNR,  $c_0 \approx 7 \times 10^{-3}$ , is more than an order of magnitude higher than its analog for the 2D case,  $c_0^{(2D)} \approx 4 \times 10^{-4}$  [16]. This can be explained by the higher and almost constant low-energy DOS for the 1D Dirac-like modes:  $\rho(\epsilon) \approx \rho(0) \sim 1$ , compared to its linear in  $\epsilon$  smallness for the 2D Dirac modes:  $\rho_{2D}(\epsilon) \approx 4\epsilon/(\pi\sqrt{3}) \ll 1$ .

Another difference is in behaviors of  $\epsilon_F(c)$  for each system, also caused by that of DOS. From Eq. (31), its almost linear growth in AGNR,  $\epsilon_F(c) \approx c/\rho(0)$ , is much slower than the extremely fast initial growth of  $\epsilon_F^{(2D)}(c) \approx \sqrt{c\pi\sqrt{3}}/2$  in 2D graphene. This defines a much higher threshold in  $c$  for occurrence of MIT in AGNR,  $c_1 \sim \epsilon_{res}\rho(0)$ , than in 2D graphene,  $\sim c_0^{(2D)}$ . But the constancy of AGNR DOS, even in the presence of impurities, permits the linear  $\epsilon_F(c)$  growth to persist also for  $c > c_1$  and then an inverse MIT to occur at its emergence from the mobility gap at  $c = c_2 \sim \epsilon_{res}\rho(0) + (\omega\rho(0))^2$ . On the contrary, the presence of a sharp impurity resonance peak in the 2D graphene DOS near  $\epsilon_{res}$  fixes the Fermi level near this peak (see the lower panel in Fig. 6) and so the insulating phase for all  $c$  above the extremely low  $c_0^{(2D)}$ . At least, the critical concentration  $c_0$  by Eq. (28) that defines the onset of localization near  $\epsilon_{res}$  indicates it to occur earlier for weaker impurity-host coupling  $\omega$ .

## V. ELECTRONIC PHASE STATES AND THEIR TUNING

An important physical issue is to determine the system electronic phase states. For the considered nanoribbons, this refers first of all to their electric conductivity.

In the limit of zero temperature, it is fully defined by the Fermi level position with respect to the spectrum mobility edges: implying the metallic phase state for  $\epsilon_F$  out of the

mobility gaps and the insulating phase state for  $\varepsilon_F$  inside them. Thus, from the diagram in Fig. 6, the system of 5-AGNR with given concentration  $c$  of Cu impurities is expected to be metallic if  $0 < c < c_1$  or  $c > c_2$  and insulating if  $c_1 < c < c_2$ .

But a practical interest arises in an effective tuning of possible MITs at a given impurity composition (in analogy with the common gate controls in doped semiconductors). First of all, the initial composition can be chosen to set the Fermi level close enough to a mobility edge, for instance,  $\varepsilon_{res} > \varepsilon_F > \varepsilon_g$  and  $\varepsilon_F - \varepsilon_g \ll \varepsilon_{res}$ . Then, for tuning of the insulator/metal transition, several factors can be considered: (1) temperature,  $T$ ; (2) magnetic field,  $\mathbf{h}$ ; and (3) electric field,  $\mathbf{E}$ .

The temperature control will result from the interplay between the metallic conductivity  $\sigma_{met}(T)$  due to extended states and the hopping conductivity  $\sigma_{hop}(T)$  due to localized states. The first type refers to the Kubo-Greenwood formula, written here as

$$\sigma_{met}(T) \approx \rho(0) \int_0^{\varepsilon_g} \tau(\varepsilon) \left[ 1 - \left( \frac{\varepsilon}{2} \right)^2 \right] \frac{\partial n(\varepsilon, T)}{\partial \varepsilon} d\varepsilon, \quad (32)$$

where the lifetime  $\tau(\varepsilon)$  is the inverse of the sum of two inverses,  $\tau_{imp}^{-1}(\varepsilon) = c |\text{Im } T(\varepsilon)|$ , from impurities, and  $\tau_{ph}^{-1}(\varepsilon) \sim T/\Theta_D$ , from 1D phonons (with the Debye temperature  $\Theta_D$ ), and  $n(\varepsilon, T) = (e^{(\varepsilon - \varepsilon_F)/T} + 1)^{-1}$  is the standard Fermi function.

The second type refers to the Mott formula written for a 1D system:

$$\sigma_{hop}(T) \propto \exp \left[ - \left( \frac{T_0}{T} \right)^{1/2} \right], \quad (33)$$

where  $T_0 \sim \tau^{-1}(\varepsilon_F)/\rho(\varepsilon_F)$ . Addition of this growing  $\sigma_{hop}(T)$  to the decreasing  $\sigma_{met}(T)$  by Eq. (32) results in an overall conductivity maximum at  $T \sim |\varepsilon_F - \varepsilon_g|$ , but having a comparable temperature width. So this crossover between the types of conductivity is not yet a canonical phase transition.

But a true electronic phase transition at  $T = 0$  can be reached, for instance, by applying a uniform static magnetic field  $\mathbf{h}$  to AGNR. This will produce a spin splitting of the Dirac-like subbands defined in Sec. III and also of the impurity levels, implying respective splitting of IRM critical points for spin subbands.

At the same time, the position of overall Fermi level for a given impurity concentration  $c$  will stay the same as it was for  $h = 0$ , due to the persisting constancy of the overall DOS. Then, in the situation of some overlapping subbands, the overall mobility edges are determined by the Mott principle: if, at a given energy, there is at least one state extended, all other states at this energy are also extended. Then the overall mobility gap is formed by the intersection of partial (formal) gaps for each spin projection and it gets reduced with growing splitting  $\mu_B h$ . In this way, the overall mobility edges are tuned by the applied field and MIT is realized at its critical value  $h_{cr} \sim |\varepsilon_F - \varepsilon_g|/\mu_B$  [see Fig. 7(a)]. But for the relevant energy scales of several millielectronvolts, this may require high enough  $h$  values of several tens Tesla.

An alternative way may be sought in applying a static electric field  $E_y \equiv E$  across the nanoribbon (along the  $y$  axis in Figs. 1 and 4) to produce linearly growing local potentials  $V_m = m e E$  on  $m$  layers. This can be shown not to influence

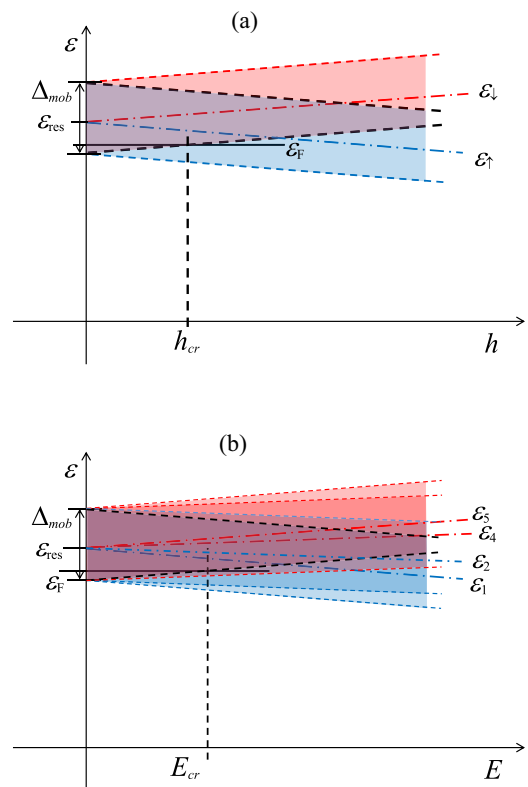


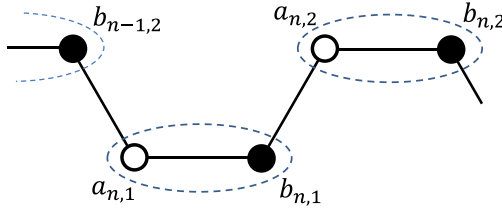
FIG. 7. Realization of MIT in AGNR with Cu top impurities by tuning of the composed mobility edges: (a) with an applied magnetic field or (b) with an applied electric field (here for  $M = 5$ ).

the relevant Dirac-like subbands, however, but to produce an  $M$ -fold splitting between the local energy levels for impurities on different  $m$  layers and so between the respective mobility gaps, with a subsequent decrease of the resulting mobility gap [as in Fig. 7(b)]. The critical fields to achieve MIT in this case,  $E_{cr} \sim |\varepsilon_F - \varepsilon_g|/(eM)$  of some mV/nm, could be reached without experimental difficulties.

## VI. SPIN-ORBIT EFFECTS ON ELECTRONIC PHASE STATES

Yet one more tuning mechanism can result from the spin-orbit (SO) effect, including the Rashba spin-orbit coupling [19]. The latter is generally known to lift the spin degeneracy in the systems with broken mirror symmetry, for instance, under electric field  $E_z$ , applied normally to the crystal surface [20] or to the 2D graphene plane (along the  $z$  axis in Fig. 4) [21,22]. A similar effect can be achieved in graphene nanotubes [23,24] and also in AGNRs [25].

For the AGNR case, we note that the relevant Dirac-like  $\psi_{\pm,k}$  modes [from Eq. (23)] have their amplitudes  $\sin m\frac{\pi}{3}$  equal zero at each third  $m$  layer, so the inter-layer couplings through these modes are restricted to the  $m$  pairs:  $(1, 2), (4, 5), \dots, (M-1, M)$ , and their overall effect on AGNR can be represented by a single such pair, for instance, with  $m = 1, 2$  (see Fig. 8). All the couplings in this pair of layers are suitably presented in terms of local operators, now equipped with explicit  $\uparrow\downarrow$  spin indices and then composed


 FIG. 8. Coupled pair of  $m = 1, 2$  layers in AGNR.

into 4-spinors:

$$f_{n,m} = \begin{pmatrix} a_{n,m,\uparrow} \\ a_{n,m,\downarrow} \\ b_{n,m,\uparrow} \\ b_{n,m,\downarrow} \end{pmatrix}. \quad (34)$$

In the basis of these local spinors, the SO Hamiltonian reads

$$H_{SO} = \sum_n [f_{n,1}^\dagger \hat{H}_{SO}(f_{n,1} + f_{n,2} + f_{n-1,2}) + f_{n,2}^\dagger \hat{H}_{SO}(f_{n,2} + f_{n,1} + f_{n+1,1})], \quad (35)$$

where the  $4 \times 4$  matrix,

$$\hat{H}_{SO} = \Delta \hat{\sigma}_z + \lambda(\hat{\sigma}_x \hat{\tau}_y - \hat{\sigma}_y \hat{\tau}_x),$$

includes the Pauli matrices  $\hat{\sigma}_j$  in spin  $\uparrow, \downarrow$  indices,  $\hat{\tau}_j$  in sublattice  $a, b$  indices, and the parameters  $\Delta$  for standard SO and  $\lambda$  for Rashba SO (the latter being  $E_z$  dependent). The estimates for these local SO couplings in 2D graphene (also plausible for nanoribbons) show the standard  $\Delta \sim 10^{-4}$  [21], fixed and much smaller of the relevant energy scales for MIT crossing. Otherwise, the Rashba  $\lambda$  can be strongly enhanced [26] and yet tunable [21], so it is taken to be an effective SO variable below.

Next we move on to the basis of chain-wave 4-spinors:

$$\psi_k = \begin{pmatrix} \psi_{+,k,\uparrow} \\ \psi_{+,k,\downarrow} \\ \psi_{-,k,\uparrow} \\ \psi_{-,k,\downarrow} \end{pmatrix}, \quad (36)$$

which are related to the local spinors by Eq. (34) (with  $m = 1, 2$ ) through a  $\hat{\tau}$  rotation:

$$f_{n,m} = \frac{(-1)^{m-1}}{2\sqrt{fN}} \sum_k e^{ik\xi_{n,m}} \hat{U}_k \psi_k. \quad (37)$$

Here the rotation matrix,

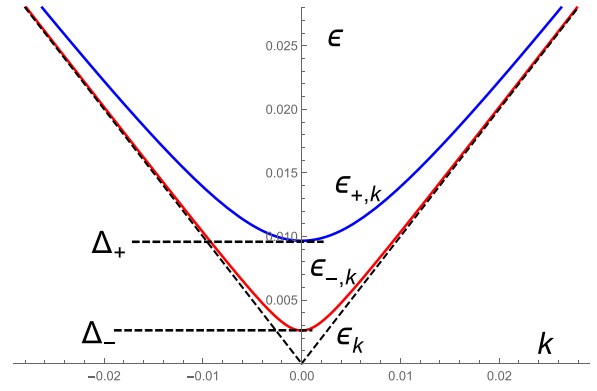
$$\hat{U}_k = \cos \phi_k (\hat{\tau}_x - \hat{\tau}_z) + \sin \phi_k (\hat{\tau}_y + i\hat{\tau}_0), \quad (38)$$

results from Eq. (11) (restricted to single  $j = 2\nu$ ) for the components of  $f_{n,m}$ . The phase  $\phi_k \equiv \phi_{2f,k}$  approximates for  $|k| \ll 1$  as  $\phi_k \approx \phi_0 = -\pi/4$ . Then the Dirac-like part of the SO Hamiltonian reads

$$H_{SO} = \sum_k \psi_k^\dagger [-\Delta \hat{\sigma}_z \hat{\tau}_x + \lambda(\hat{\sigma}_x \hat{\tau}_z + \hat{\sigma}_y \hat{\tau}_y)] \psi_k, \quad (39)$$

and, together with the Dirac-like part of  $H_{tb}$  by Eq. (10), it defines the SO-split dispersion laws (in neglect of impurity disorder):

$$\varepsilon_{\pm,k} = \sqrt{\varepsilon_k^2 + \Delta_{\pm}^2}. \quad (40)$$


 FIG. 9. SO splitting of the Dirac-like mode  $\varepsilon_k$  (dashed lines) into  $\varepsilon_{\pm,k}$  at the choice of  $\lambda = 5 \times 10^{-3}$  and  $\Delta = 2.5 \times 10^{-4}$ .

Here the nonzero band gaps are due to both SO types, but their splitting is only due to the Rashba SO:

$$\Delta_{\pm} = \sqrt{\Delta^2 + \lambda^2(2 \pm \sqrt{3})}, \quad (41)$$

as shown in Fig. 9 for the choice of SO parameters  $\Delta = 2.5 \times 10^{-4}$  [21] and  $\lambda = 5 \times 10^{-3}$  [26], and they create the low-energy DOS singularities:

$$\rho_{so}(\varepsilon) = \frac{\varepsilon \rho(0)}{2} \left[ \frac{\theta(\varepsilon - \Delta_+)}{\sqrt{\varepsilon^2 - \Delta_+^2}} + \frac{\theta(\varepsilon - \varepsilon_-)}{\sqrt{\varepsilon^2 - \Delta_-^2}} \right], \quad (42)$$

as shown in Fig. 10.

Such DOS behavior, instead of its almost constancy at no account of SO [by Eq. (22)], when used in Eq. (31) leads to the  $\lambda$  dependence of the Fermi level given by the equation

$$\sqrt{\varepsilon_F^2 - \varepsilon_+^2} + \sqrt{\varepsilon_F^2 - \Delta_-^2} \approx c/\rho(0). \quad (43)$$

Its numerical solution shown in Fig. 11 defines MIT to occur when  $\lambda$  reaches a certain critical value  $\lambda_{cr}$ .

Noting that for all relevant impurity concentrations  $c > c_0$  we have  $c/\rho(0) \gg \Delta$ , the approximate solution of Eq. (43) for  $\lambda \ll c/\rho(0)$  reads

$$\varepsilon_F(\lambda) \approx \frac{c}{2\rho(0)} + \frac{\rho(0)}{c} \Delta^2 + \frac{2\rho(0)}{c} \lambda^2. \quad (44)$$

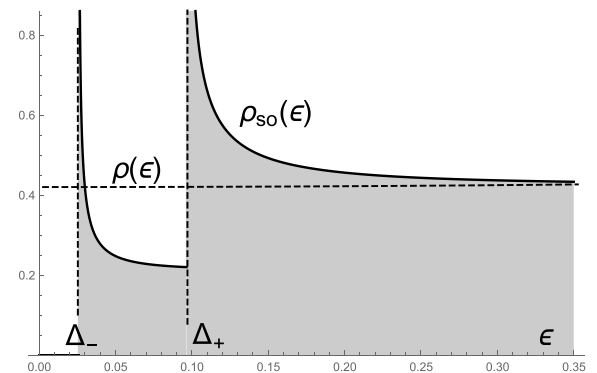


FIG. 10. Singularities of the low-energy DOS of 5-AGNR with split subbands at the same choice of SO parameters as in Fig. 9.

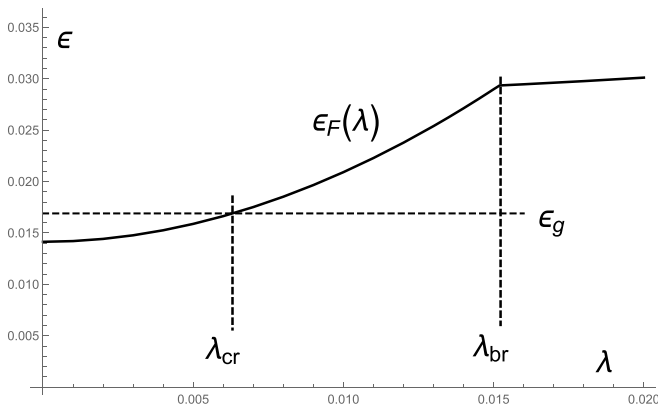


FIG. 11. Dependence of the Fermi level on Rashba SO coupling for 5-AGNR with Cu top impurity concentration fixed at  $c = 0.012$ . Its crossing with the mobility edge  $\varepsilon_g$  at  $\lambda = \lambda_{cr}$  indicates an SO-tuned MIT to occur.

This quadratic  $\lambda$  dependence relates to filling of both  $\varepsilon_{\pm,k}$  subbands by  $c$  charge carriers. It practically coincides with the lower part of the numerical solution in Fig. 11 until its break, which occurs when  $\varepsilon_F(\lambda)$  gets intercepted by the faster-growing upper band gap  $\varepsilon_+$  at the break value  $\lambda_{br} = c/[\sqrt{2}\sqrt{3}\rho(0)]$ . The next slower  $\varepsilon_F(\lambda)$  growth at  $\lambda > \lambda_{br}$  relates to filling of only the lower subband as

$$\varepsilon_F(\lambda) = \sqrt{\frac{c^2}{\rho(0)^2} + \Delta^2 + (2 - \sqrt{3})\lambda^2}. \quad (45)$$

Notably, for the considered case of Cu top impurities, both the impurity resonance  $\varepsilon_{res}$  and the mobility edge  $\varepsilon_g$  lie in the energy range  $\varepsilon \gg \varepsilon_{\pm}$  where  $\rho_{SO}(\varepsilon)$  already reaches its asymptote  $\approx \rho(0)$ , so the mobility gap structure stays practically insensitive to Rashba SO. Hence a possibility arises here for MIT to be realized by SO tuning of  $\varepsilon_F$  at fixed  $\varepsilon_g$ , unlike the above-considered regimes with tuning of mobility edges at fixed Fermi level.

Notably, this tuning process can be realized in a combined way: a rough “tuning” of  $\varepsilon_F$  closeness to  $\varepsilon_g$  by a proper choice of impurity parameters  $\varepsilon_{res}$ ,  $\omega$ ,  $c$  and also by a strong structural contribution to the Rashba parameter  $\lambda$ , say, from a gold substrate atomic field [26], and then its fine tuning by an applied external field. Evidently, the expected MIT at such sub-meV energy scales would require a range of liquid He temperatures for its sufficient resolution.

## VII. DISCUSSION

The obtained results demonstrate how the difference of electronic states in graphene nanoribbons defined by their edge orientations is reflected in their stability against impurity disorder. Physically, this opens the possibility for specific electronic phase transitions and for their controls, e.g., by combining the disorder and external bias effects.

The present study was limited to the simplest framework of tight-binding model for pure nanoribbons and to

the simplest models for impurity perturbations on them. But it already reveals a qualitative distinction between the isotopic-type and hybrid-type perturbations in the aspect of quasiparticle localization. Moreover, the results obtained here for the simplest top position of impurity adatoms should qualitatively hold also for their bridge or hole positions (by similarity of the respective AM parameters [16]). In principle, this approach can be extended to account for many other physical factors, such as electron-electron Hubbard correlations, spin-ordering effects, phonon and magnon quasiparticles, etc.

Also, the effects from passivating hydrogens, known to be commonly present at the edges of experimental nanoribbon samples [27–30], may influence the dynamics of host nanoribbon carriers. This factor can be naturally included into the above-developed Hamiltonians and resulting GFs, to be possibly an object of future study. At least, an experimental check for the suggested effects, for instance, on carrier mobility and its collapse under definite external factors, should be of considerable interest.

## ACKNOWLEDGMENTS

We are grateful to Larissa S. Brizhik, Mark I. Dykman, and Aleksandr A. Eremko for useful discussions of this work. The work by V.M.L. was partially supported by Grant No. 0122U000887 from the Department of Physics and Astronomy of the National Academy of Sciences of Ukraine.

## APPENDIX: BEYOND THE T MATRIX

Validity of the above T-matrix solution should be yet verified in view of the effective 1D character of the relevant Dirac-like quasiparticles. It is known that generic 1D systems are unstable against any disorder, producing full localization of all their eigenstates [31], and the IRM check with use of the simplest (single-impurity) T matrix does not detect this. Therefore the IRM results from Sec. III need a support by some T-matrix extensions known for many other disordered systems. There are two such possible extensions:

- (1) group expansions (GEs) in clusters of correlated impurity centers [32] and
- (2) self-consistent T-matrix approximation [33].

For GEs, their basic elements are the correlators, defined for different GE forms. The simplest form is that of nonrenormalized GE, known to better apply for the energy ranges of localized states. Here the correlator for the considered Dirac-like quasiparticles is written as

$$A_r(\varepsilon) = \frac{2T(\varepsilon)}{3vN} \sum_k e^{ikr} \left( \frac{1}{\varepsilon - \varepsilon_k} + \frac{1}{\varepsilon + \varepsilon_k} \right) \quad (A1)$$

(taking into account equal contributions from  $j = v$  and  $j = 2v$  modes). Then, after integration in  $k$  by Eq. (20), the related integral has its long-distance asymptotics at  $r \gg 1$  as

$$A_r(\varepsilon) = \frac{2T(\varepsilon)\varepsilon}{3\pi v} \int_{-\pi}^{\pi} \frac{e^{ikr} dk}{\varepsilon^2 - 4 \sin^2 k/2} \approx \frac{2T(\varepsilon)\varepsilon}{3f} \sin \varepsilon r, \quad (A2)$$

which is nondecaying. This contrasts with the decaying correlators in 3D and 2D systems and makes all the

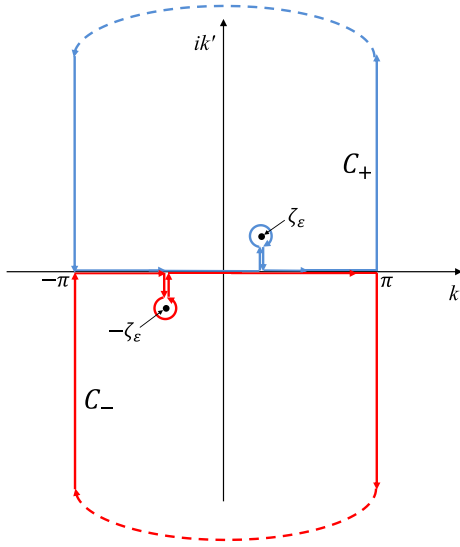


FIG. 12. Integration contours for calculation of the renormalized correlator  $\tilde{A}_r(\varepsilon)$ , Eq. (A3):  $C_+$  (blue lines) for  $r > 0$  and  $C_-$  (red lines) for  $r < 0$ .

GE terms for the 1D-like system formally divergent. To avoid that problem, some alternative, renormalized GE forms (more adequate for conductive states) could be employed.

For instance, the first-order renormalization for GE is obtained with the simple change,  $\varepsilon \rightarrow \varepsilon - cT(\varepsilon)$  in the denominators of Eq. (A1). Then the renormalized correlator,  $\tilde{A}_r(\varepsilon) = 2T(\varepsilon)[\varepsilon - cT(\varepsilon)]\tilde{I}_r(\varepsilon)/(3\nu)$ , involves the integral

$$\tilde{I}_r(\varepsilon) = \frac{1}{2\pi} \int_{-\pi}^{\pi} \frac{e^{ikr} dk}{[\varepsilon - cT(\varepsilon)]^2 - 4\sin^2 k/2}. \quad (\text{A3})$$

This can be found analytically, passing to complex momentum  $k \rightarrow \zeta = k + ik'$  and extending integration to one of the closed contours shown in Fig. 12, depending on the 1D correlator direction. The forward direction,  $r > 0$ , relates to  $C_+$  (blue lines) with the pole  $\zeta_\varepsilon = 2 \arcsin[\varepsilon - cT(\varepsilon)]/2$ , and the

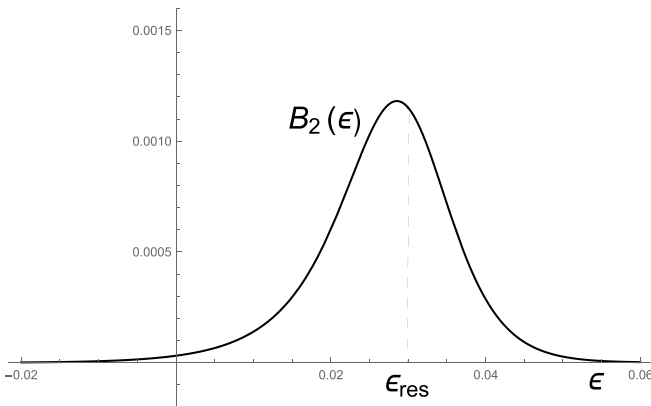


FIG. 13. Smallness of the relative contribution to GE by impurity pairs  $B_2(\varepsilon)$  by Eq. (A8) (for Cu impurities with concentration  $c = 0.05$  in 5-AGNR), assuring GE convergence for this system.

backward direction,  $r < 0$ , does to  $C_-$  (red lines) with the pole  $-\zeta_\varepsilon$ .

The contour integral for the forward case,

$$\frac{1}{2\pi} \oint_{C_+} \frac{e^{i\zeta r}}{\varepsilon - cT(\varepsilon) - 2\sin \zeta/2} d\zeta, \quad (\text{A4})$$

presents a zero sum of three terms:  $0 = I_r(\varepsilon) + R_r(\varepsilon) + V_r(\varepsilon)$ . Here the residue term,  $R_r(\varepsilon) = e^{i\zeta_\varepsilon r} / \cos(\zeta_\varepsilon/2)$ , and the term from the semi-infinite vertical segments,  $V_r(\varepsilon) \approx (2i \sin \pi r) / [(1 - \varepsilon)r]$ , define the sought correlator as

$$\tilde{A}_r(\varepsilon) = \frac{2T(\varepsilon)[\varepsilon - cT(\varepsilon)]}{3f} \left[ \frac{e^{i\zeta_\varepsilon r}}{\cos(\zeta_\varepsilon/2)} + 2i \frac{\sin \pi r}{(1 - \varepsilon)r} \right]. \quad (\text{A5})$$

For the low-energy range,  $|\varepsilon|, c|T(\varepsilon)| \ll 1$  and  $\zeta_\varepsilon \approx \varepsilon - cT(\varepsilon)$ , Eq. (A5) simplifies to

$$\tilde{A}_r(\varepsilon) \approx \frac{2T(\varepsilon)[\varepsilon - cT(\varepsilon)]}{3\nu} \times \left[ e^{i[\varepsilon - c\text{Re} T(\varepsilon)]r} e^{-c|\text{Im} T(\varepsilon)r|} + 2i \frac{\sin \pi r}{r} \right]. \quad (\text{A6})$$

Here, unlike Eq. (A2), both terms in the brackets are already decaying with  $r$ . For the backward case, integration over  $C_-$  gives the same result.

The relevant criterion for GE convergence is smallness of the dominating contribution by impurity pair clusters into the quasiparticle self-energy compared to that by single impurities [32]:

$$B_2(\varepsilon) \approx c \left| \int_0^\infty \tilde{A}_{-r}(\varepsilon) \tilde{A}_r(\varepsilon)^2 e^{-i[\varepsilon - c\text{Re} T(\varepsilon)]r} dr \right| \ll 1. \quad (\text{A7})$$

Then the residue term in Eq. (A6) with its slower exponential decay  $\propto e^{-c|\text{Im} T(\varepsilon)r|}$  dominates in the  $r$  integral and converts the above criterion into

$$B_2(\varepsilon) \approx \frac{8}{81\nu^3} \left| \frac{T^3(\varepsilon)[\varepsilon - cT(\varepsilon)]^3}{\text{Im} T(\varepsilon)} \right| \ll 1. \quad (\text{A8})$$

The straightforward numerical check shows this criterion to surely hold for all the above-considered impurity parameters (see an example in Fig. 13).

Also, the self-consistent extension of the T-matrix function,

$$T_{sc}(\varepsilon) = \frac{\omega^2}{2} \left\{ \varepsilon - \varepsilon_{res} - \frac{i\omega^2}{4\nu \sqrt{1 - \left[ \frac{\varepsilon - cT_{sc}(\varepsilon)}{2} \right]^2}} \right\}, \quad (\text{A9})$$

practically coincides with its nonrenormalized version  $T(\varepsilon)$  by Eq. (25), due to the above-noted smallness of  $|\varepsilon - cT(\varepsilon)| \ll 1$ , assured for all  $|\varepsilon| \ll 1$ .

Hence the discussed T-matrix results for the quasiparticle spectra in disordered AGNRs and the related estimates for their mobility edges can be considered valid. We conclude that the inverse lifetime by the nonrenormalized T matrix in the right-hand side of Eq. (30) is the main factor for quasiparticle localization in AGNRs. So the results of Sec. III correctly determine the system observable characteristics.

- [1] K. S. Novoselov, A. K. Geim, S. V. Morozov, S. V. Dubonos, Y. Zhang, and D. Jiang, [arXiv:cond-mat/0410631](https://arxiv.org/abs/cond-mat/0410631) (2004).
- [2] S. V. Morozov, K. S. Novoselov, F. Schedin, D. Jiang, A. A. Firsov, and A. K. Geim, *Phys. Rev. B* **72**, 201401(R) (2005).
- [3] A. H. Castro Neto, F. Guinea, N. M. R. Peres, K. S. Novoselov, and A. K. Geim, *Rev. Mod. Phys.* **81**, 109 (2009).
- [4] L. Yang, C.-H. Park, Y.-W. Son, M. L. Cohen, and S. G. Louie, *Phys. Rev. Lett.* **99**, 186801 (2007).
- [5] X. Yang, X. Dou, A. Rouhanipour, L. Zhi, H. J. Räder, and K. Müllen, *J. Am. Chem. Soc.* **130**, 4216 (2008).
- [6] P. Ruffieux, J. Cai, N. C. Plumb, L. Pattney, D. Prezzi, A. Ferretti, E. Molinari, X. Feng, K. Müllen, C. A. Pignedoli, and R. Fasel, *ACS Nano* **6**, 6930 (2012).
- [7] M. Fujita, K. Wakabayashi, K. Nakada, and K. Kusakabe, *J. Phys. Soc. Jpn.* **65**, 1920 (1996).
- [8] Y. G. Pogorelov, D. Kochan, and V. M. Loktev, *Low Temp. Phys.* **47**, 754 (2021).
- [9] K. Wakabayashi, Y. Takane, M. Yamamoto, and M. Sigrist, *New J. Phys.* **11**, 095016 (2009).
- [10] K. Wakabayashi, K. Sasaki, T. Nakanishi, and T. Enoki, *Sci. Technol. Adv. Mater.* **11**, 054504 (2010).
- [11] D. Zubarev, *Sov. Phys. Usp.* **3**, 320 (1960).
- [12] E. N. Economou, *Green's Functions in Quantum Physics* (Springer, New York, 1979).
- [13] I. M. Lifshitz, *Sov. Phys. JETP* **17**, 1159 (1963).
- [14] P. W. Anderson, *Phys. Rev.* **124**, 41 (1961).
- [15] V. L. Bonch-Bruевич and S. V. Tyablikov, *The Green Function Method in Statistical Mechanics* (North Holland Publishing House, Amsterdam, 1962).
- [16] Y. G. Pogorelov, V. M. Loktev, and D. Kochan, *Phys. Rev. B* **102**, 155414 (2020).
- [17] A. F. Ioffe and A. R. Regel, *Prog. Semicond.* **4**, 237 (1960).
- [18] N. F. Mott, *Phil. Mag.* **19**, 835 (1969).
- [19] Yu. A. Bychkov and E. I. Rashba, *JETP Lett.* **39**, 78 (1984).
- [20] F. T. Vas'ko, *JETP Lett.* **30**, 541 (1979).
- [21] C. L. Kane and E. J. Mele, *Phys. Rev. Lett.* **95**, 226801 (2005).
- [22] F. Kuemmeth and E. I. Rashba, *Phys. Rev. B* **80**, 241409(R) (2009).
- [23] D. Huertas-Hernando, F. Guinea, and A. Brataas, *Phys. Rev. B* **74**, 155426 (2006).
- [24] M. S. Rudner and E. I. Rashba, *Phys. Rev. B* **81**, 125426 (2010).
- [25] L. Lenz, D. F. Urban, and D. Bercioux, *Eur. Phys. J. B* **86**, 502 (2013).
- [26] D. Marchenko, A. Varykhalov, M. R. Scholz, G. Bihlmayer, E. I. Rashba, A. M. Shikin, and O. Rader, *Nat. Commun.* **3**, 1 (2012).
- [27] S. Wang, L. Talirz, C. A. Pignedoli, X. Feng, K. Müllen, V. Meunier, R. Fasel, and P. Ruffieux, *Nat. Commun.* **7**, 11507 (2016).
- [28] P. Ruffieux, S. Wang, B. Yang, C. Sanchez-Sánchez, J. Liu, T. Dienel, L. Talirz, P. Shinde, C. A. Pignedoli, D. Passerone, T. Dumslaff, X. Feng, K. Müllen, and R. Fasel, *Nature (London)* **531**, 489 (2016).
- [29] S. Wang, N. Kharche, E. Costa Girão, X. Feng, K. Müllen, V. Meunier, R. Fasel, and P. Ruffieux, *Nano Lett.* **17**, 4277 (2017).
- [30] M. El Abbassi, M. L. Perrin, G. Borin Barin, S. Sangtarash, J. Overbeck, O. Braun, C. J. Lambert, Q. Sun, T. Prechtl, A. Narita, K. Müllen, P. Ruffieux, H. Sadeghi, R. Fasel, and M. Calame, *ACS Nano* **14**, 5754 (2020).
- [31] I. M. Lifshits, S. A. Gredeskul, and L. A. Pastur, *Introduction to the Theory of Disordered Systems* (Wiley, New York, 1988).
- [32] M. A. Ivanov, V. M. Loktev, and Yu. G. Pogorelov, *Phys. Rep.* **153**, 209 (1987).
- [33] R. J. Elliott, J. A. Krumhansl, and P. L. Leath, *Rev. Mod. Phys.* **46**, 465 (1974).